This manuscript is a preprint and will be shortly submitted for publication to a scientific journal. As a function of the peer-reviewing process that this manuscript will undergo, its structure and content may change. If accepted, the final version of this manuscript will be available via the 'Peer-reviewed Publication DOI' link on the right-hand side of this webpage. Please feel free to contact any of the authors; we welcome feedback.

Mapping landslides through a temporal lens: An insight towards multi-temporal landslide mapping using the U-Net deep learning model

Kushanav Bhuyan [1,2], Sansar Raj Meena [1,2 *], Lorenzo Nava [1], Cees van Westen[2], Mario Floris [1], and Filippo Catani [1]

[1] Machine Intelligence and Slope Stability Laboratory, Department of Geosciences, University of Padova, 35129 Padua, Italy.

[2] Faculty of Geo-information Science and Earth Observation (ITC), University of Twente, 7514 AE Enschede, Netherlands.

*Corresponding author: Kushanav Bhuyan (k.bhuyan@utwente.nl)

Abstract

Repeated temporal mapping of landslides is essential for investigating changes in landslide movements, legacy effects of the landslide triggering events, and susceptibility changes in the area. However, in order to perform such investigations, multi-temporal (MT) inventories of landslides are required. The traditional approach of visual interpretation from cloud-free optical remote sensing imageries is time consuming and expensive. Recent endeavours exploring Convolutional Neural Networks and deep learning models have made rapid and accurate mapping of landslides feasible but have not been applied for multi-temporal landslide mapping in the Himalayas, yet. Earlier models used a standard supervised learning approach, with a small landslide inventory over a limited area used for training , which is then utilized to predict landslides in nearby areas. We propose a new strategy, using geographically separate training samples to design a standard approach which can be utilized to create multi-temporal landslide inventories. RapidEye images of 5-metres spatial resolution are used to generate MT landslide inventories in the study area of Rasuwa district, Nepal. We test the effectiveness of the model by training with only 55 landslides and predicting for a different area. Then, using the weights attained from this first training phase, we use transfer learning to map landslides over a time period between 2013 and 2019 in the Rasuwa district. We also adopt data augmentation techniques to add more training samples, leading to higher overall accuracies ranging from 58% in 2015 to 80% in 2017. We also perform a spatial comparison between the manual (observed) and predicted inventories to evaluate the differences between landslide densities and overall landslide statistics of landslide area distribution. The benefit of a transfer learning-based model training is that it circumvents the need for generating annual inventories for training a deep learning. A single event based inventory is enough to generate landslide inventories over a number of years, at least until landslide preparatory conditions do not change significantly. This application can enable automated workflows to generate MT landslide inventories of particular areas as the basis for landslide evolution and movement change analysis.

Keywords: Multi-temporal, Deep Learning, U-Net, Nepal, Landslide inventories

Highlights

- First artificial intelligence model to map landslides over time.
- Mapping of pre-, co-, and post-seismic landslides of the Gorkha earthquake event of 2015.
- Releasing source codes for the methodology along with the predicted inventories.

1. Introduction

Landslides are major causes of loss to life, livelihood, and property due to their destructive nature and dynamic behaviour. The crucial roles of triggering factors like rainfall, earthquakes, and anthropogenic activities, accompanied by the intrinsic factors of slope, soil characteristics, and geomorphic process contribute to slope failures (Serey et al., 2019; Wang et al., 2019).

Landslide inventories are the foundation for evaluating the hazard and risk induced by land sliding (Van Westen, Ghosh, Jaiswal, Martha, & Kuriakose, 2013; Metternicht, Hurni, & Gogu, 2005; Soeters & Van Westen, 1996; Sreedevi & Yarrakula, 2016). With the help of inventories, we can store crucial information related to the time of occurrence, type and the initiation and runout components of landslides. Incomplete and inaccurate landslide inventories can seriously affect the reliability of hazard and risk maps, and the availability of reliable and fast landslide mapping methodologies is fundamental.

In the last few years, landslide mapping has seen a rapid development with techniques using a combination of Earth Observation data, topographic factors (Ghorbanzadeh, Meena, et al., 2021a; Meena et al., 2022), and advanced machine learning (ML) and deep learning (DL) algorithms (Fang, Chen, Pan, Kou, & Wang, 2021; Prakash, Manconi, & Loew, 2020, 2021). DL algorithms, especially Convolutional Neural Networks (CNNs), have been successfully employed, demonstrating wider generalization capabilities when compared to other ML models. Ghorbanzadeh et al. (2019) used high-resolution Rapid Eye data to test several ML techniques, including support vector machines (SVMs), random forest (RF), artificial neural networks (ANNs), and deep convolutional neural networks (D-CNN), with CNNs attaining the best results. Meena et al. (2021) used a composite of optical RapidEye images and topographical maps with CNNs to obtain a mean F1-score of 78 % to map rainfall-induced landslides.

However, to comprehend the evolution of landslides in an area over time, the availability of reliable multi-temporal landslide (MTL) inventories is crucial. Moreover, MTL inventories can also help in designing rainfall thresholds based on inventories of event-based rainfall-induced landslides. Based on the assessment of rainfall thresholds obtained from evaluating rainfall circumstances that have caused landslides to occur, empirical approaches for determining the temporal probability of landslides are used (Jaiswal & van Westen, 2009). MTL inventories can also help to study the development of co-seismic landslides in the years after the earthquake and as the basis for consideration probabilistic earthquake-induced landslide hazard models (Guzzetti, Reichenbach, Cardinali, Galli, & Ardizzone, 2005; Fan et al. (2017, 2019, 2021), Tang et al. (2016), and Tanyaş et al. (2021).

However, the acquisition and generation of MTL inventories is problematic, due to the access to cloud-free satellite images, the subjectivity in mapping landslides manually, and the availability of resources and time in producing the inventories (Van Westen et al., 2006; Meena and Piralilou, 2019). When using an automated classification, the subjectivity is limited due to a unbiased mapping approach, which is also much faster, when compared to manual interpretation. Although a wide collection of landslide mapping research has been published, no model has been designed to automatically map landslides over time with artificial intelligence models thus far.

This study presents an approach to temporally map landslides, illustrated for the Mailung area of Nepal, which was affected by the 2015 Gorkha earthquake, in which large changes in landslide activity can be observed between 2013 and 2017.

2. Study area

The study area is located in central Nepal's higher Himalayan district of Rasuwa and is among the most landslide-affected region (see Figure 1). The most common land cover is forest, grassland, shrubland, farmland, and rural regions. With an annual average rainfall of 691mm, this region's climate is influenced by orographic monsoon precipitation. Landslides were triggered after the 2015 Gorkha earthquake that dammed the river, which resulted in the formation of multiple lakes behind the dams in various locations. The leading cause of severe flash floods and monsoonal rains is water obstruction behind landslide-induced dams. (see Figure 1).

Due to the Gorkha earthquake in April 2015, more than 80 lives were perished as a result of landslides and rockfalls near the hydropower project construction camps in Mailung village. The damages resulted in a drop in energy output as well as significant economic damage (Schwanghartet al., 2018). The orographic monsoon precipitation can be severe, with an annual average rainfall of about 700 mm. Landslides in the areas affected by the Gorkha earthquake were mapped by Kargel et al. (2016), Martha et al. (2016), and Roback et al. (2018). Rosser et al. (2021) also monitored the landslide evolution of new post-seismic landslides by manually generating detailed time-series landslide maps. Therefore, the preface and importance for multi-temporal mapping is witnessed and realised.

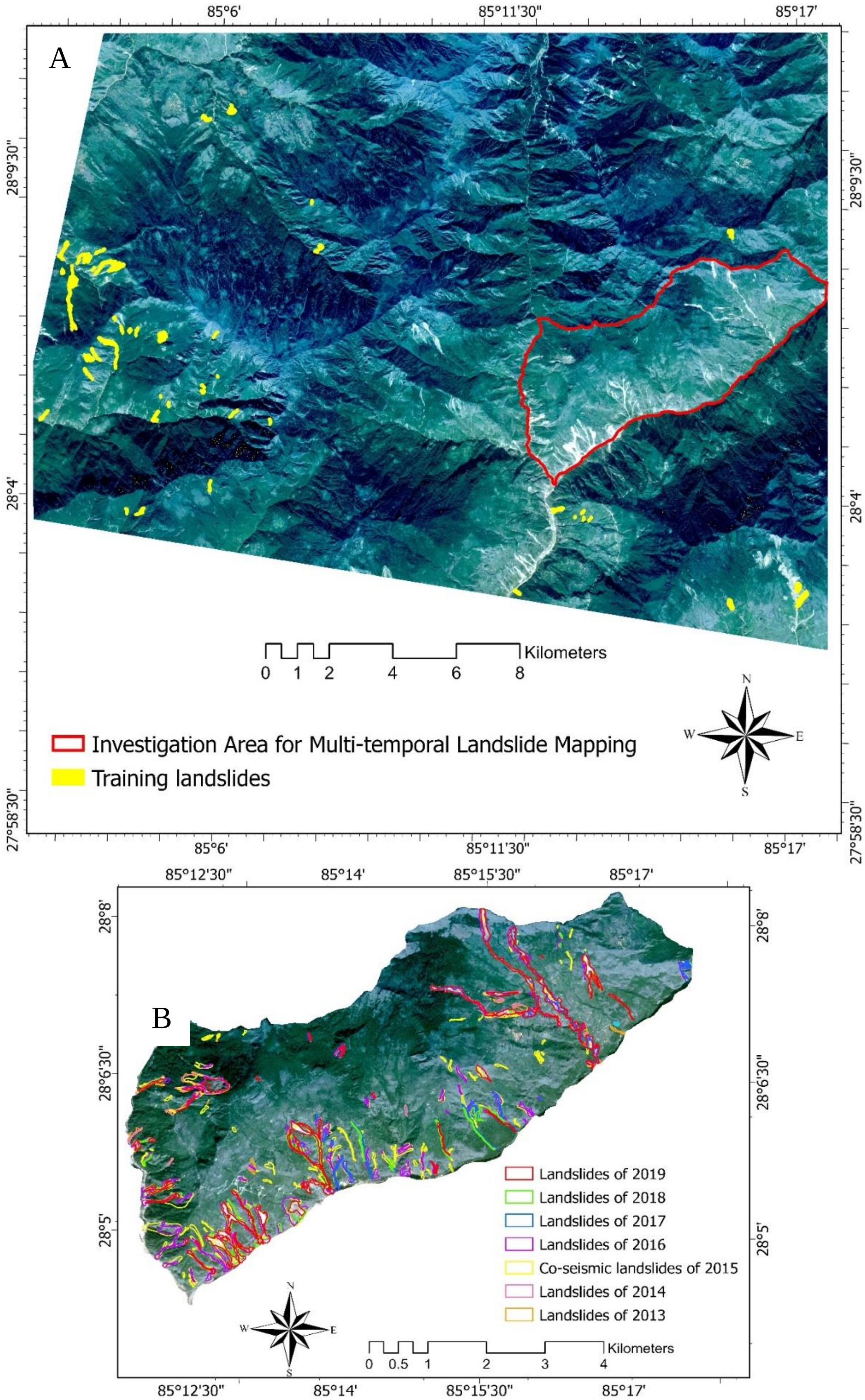

Figure 1: A: Study area location. B: MTL mapped over the years between 2013 and 2019 in the investigation area (red outline) with landslides (yellow) used as preliminary training data for the deep learning model.

3. Data used and methodology

3.1 Data sets and sampling strategy

We generated annual landslide inventories of an area of 33km² using RapidEye images from Planet Labs (Planet Team, 2017), acquired over the years between 2013 and 2019 by manually digitising the landslide polygons (Table 1). The seven satellite images have 5 metre pixel resolution and five bands of Red, Green, Blue, Red-edge, and Near-infrared. Apart from these landslide inventories, landslides were also digitised outside the investigation area (yellow polygons in Figure 1) to be used as initial training data. The conceptualisation of the research is shown in figure 2.

Table 1: Information about the satellite images from Planet and the respective landslides.

Gorkha Earthquake of 2015

	Image acquisition dates	Number of landslides	Landslide Area (m²)		
			Total	**Minimum**	**Maximum**
Pre-seismic (2013)	07-11-2013	31	513,304.8	216.3	148,948.1
Pre-seismic (2014)	30-11-2014	26	438,778.5	515.7	150,759.3
Co-seismic (2015)	09-11-2015	136	1,855,911.8	276.4	145,380.5
Post-seismic (2016)	04-11-2016	95	1,796,221.2	768.3	137,397.8
Post-seismic (2017)	12-11-2017	63	1,188,037.6	724.5	141,102.3
Post-seismic (2018)	24-10-2018	55	1,315,124.4	724.5	141,102.3
Post-seismic (2019)	10-11-2019	52	1,222,396.5	724.5	112,723.0

We mapped 55 landslides for 2016 for the first training phase which are located outside of the area of investigation (Figure 1-B red outline), to avoid bias. The To test the model's prediction capabilities, the U-Net model was trained for 250 epochs and then validated in the investigation area for the year 2016 (one year after the Gorkha earthquake). We used model checkpoint to save and choose the epoch with the best accuracies. We then applied transfer learning within the investigation area for each year from 2013 to 2019, which varies not only geographically but also temporally and spectrally. Weight initialization was unnecessary because pre-training weights were already specified. In this next phase of training, we first sampled the landslides inside the investigation area into two sets: a training set (70%) (for re-training) and a testing set (30%), and then using the pre-trained weights, we performed transfer learning by re-training the model within the investigation area and testing the model prediction capability with the test set. We also choose satellite images from the same late autumn/early winter season with low cloud cover to maintain similar spectral characteristics. Spectral differences are witnessed in the temporal image acquisitions (Anderson & Perry, 1996; Huete, 2004), and coupled with image distortions for each acquisition, modelling the landslides was a challenging task as we see later in section 4.

We extracted patches of 128 x 128 pixels from the input satellite images, as suitable input for CNNs, based on Ghorbanzadeh et al. (2021) and Prakash et al. (2021), who reported optimal accuracies of F1-score, Precision, and Recall using this patch size. By rasterizing the manual inventory of the different years with 5 meter grid cells, the associated binary masks were created. Data augmentation is also adopted to artificially expand the training samples by applying image transformations like rotation, shear, horizontal and vertical flips. These augmentations help in diversifying the training dataset and aid in regularising the model to better generalise landslide features (Kukačka, et al., 2017; Shorten and Khoshgoftaar, 2019). We applied these augmentations respectively to the satellite images and the corresponding binary masks.

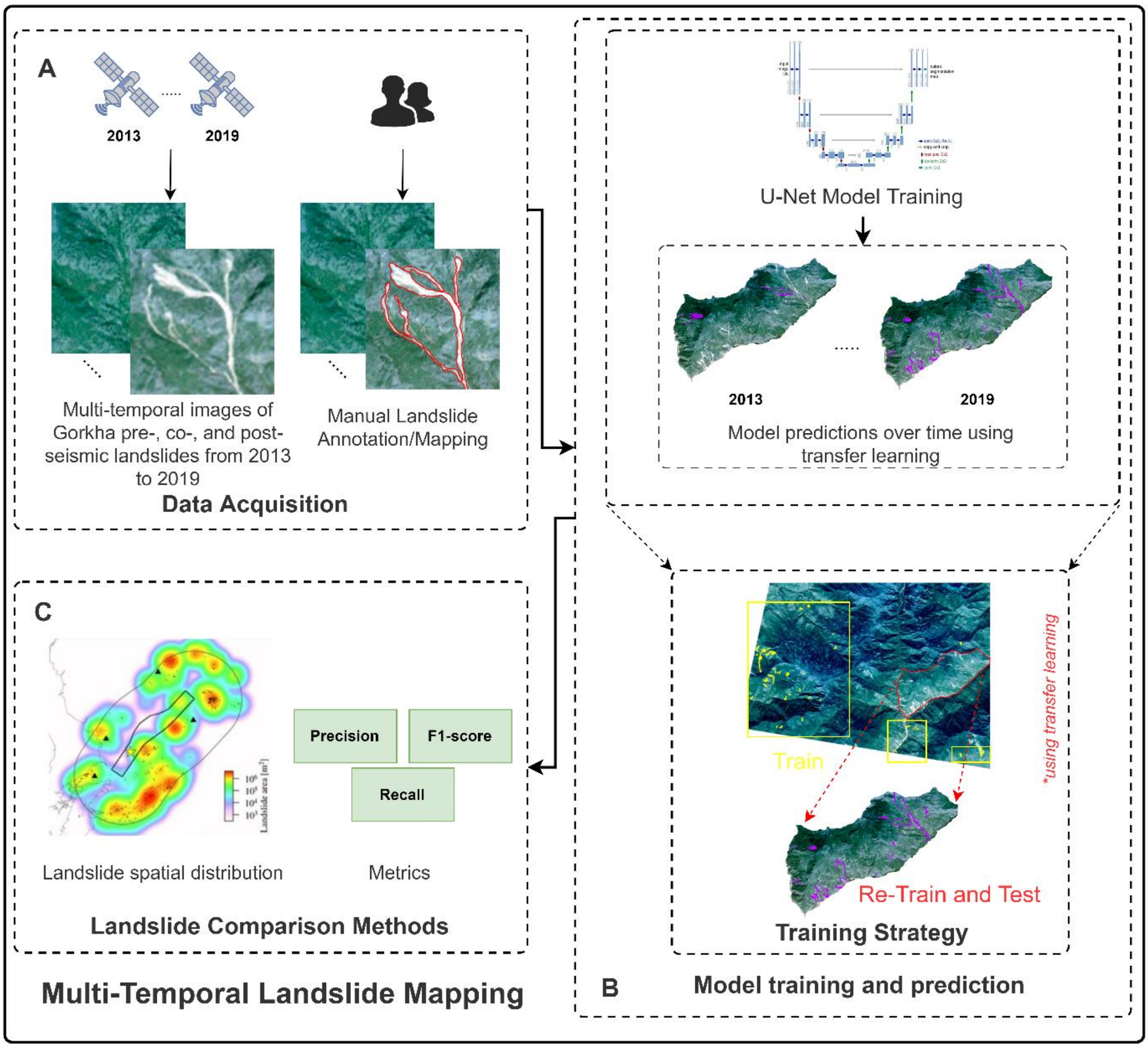

Figure 2: Conceptual diagram of the methodology. **A**: data acquisition of satellite images between 2013 and 2017, and manually annotated landslides of the same periods. **B**: model training and prediction using transfer learning. **C**: comparison methods with classical metrics and landslide spatial distribution.

3.2 U-Net Model

3.2.1 Model training and transfer learning

The U-Net model has been used extensively for landslide detection (Ronneberger, et al., 2015) due to its robust network structure and segmented pixels as outputs(Ghorbanzadeh, et al. , 2021; Prakash et al. , 2021; Zhang et al., 2018). The U-Net model (Figure 3) has many advantages. One of these is that it extracts local features through skip connections between the encoder-decoder stages. As spatial details tend to get lost at the deepest end of the encoder stages during model training, the decoder stage with the help of the skip connections retrieve the relevant spatial information from the low-level features and provides per-pixel segmented results. In this study, we use a deep U-Net model with 5 convolutional blocks containing 10 convolutional layers in total.

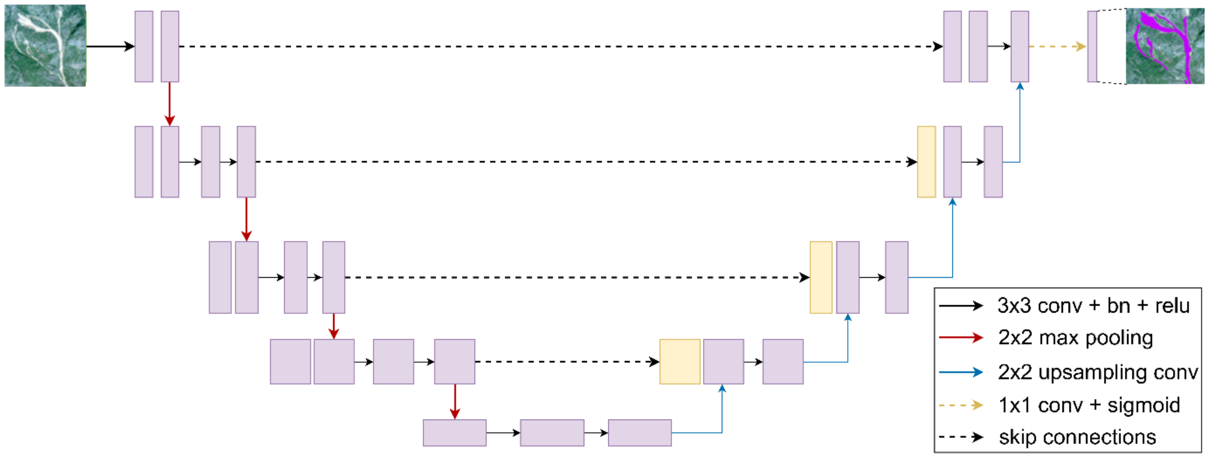

Figure 3: An overview of the U-Net model used in our research.

We adopt a transfer learning mechanism to train a temporally generalisable model that would be able to detect and map landslides over time. The goal of transfer learning is to transfer the information from previous data and apply what the model has learnt in a new environment, which might be difficult to learn in otherwise. The weights from a prior model can be used in a new region of interest, with the network learning on top of the pre-trained model and retraining an output layer using the target landslide data set. This strategy can reduce the model's training time and increase its effectiveness in a new region (Bai, Wang, Zhang, & Cheng, 2012; Xu et al., 2013).

3.2.2 Hyper-parameter tuning

In this study, the Adam optimiser was employed as advocated by Bottou (2010) and Pan et al. (2020) due the adaptive learning capability of the optimiser which allows faster convergence to decrease the loss, thereby improving model accuracy. Different learning rates are investigated as well, within the Adam optimiser, to enhance training speed and balance model overfitting. As an outcome of this stage, heat maps of probability pertaining to the classes landslides and non-landslides are generated. After training, the outcome is a binary image that differentiates between *landslides* and *non-landslides* pixels. The U-Net model training was conducted in the Python environment on an NVIDIA RTX 3060 GPU (6 GB VRAM) and 16 GB of RAM.

One of the most critical processes in regulating the model's general behaviour is hyper-parameter tuning. The aim is to identify the optimal hyper-parameter combination that minimizes the loss and produces the best result. In this study, the Tversky Loss (equation 1) (Abraham & Khan, 2019) function was applied. Using so-called beta weights, the Tversky loss has the benefit of immediately modifying and adjusting the False Positives and False Negatives. The alpha and beta parameters of the Tversky loss function regulate the false positives and false negatives, respectively, thereby impacting the overall prediction capability of the model. This parameter helps decrease model loss when training to obtain improved accuracy by adjusting the imbalance between the data within *landslides* and *non-landslides* classes.

$$Tversky\ Loss = \frac{TP+\varepsilon}{TP+\alpha\times FN+\beta\times FP+\varepsilon} \quad (1)$$

where,

TP = True Positives
FP = False Positives
FN = False Negatives
ε = A constant value of 0.0001 (by default) which prevents the loss from becoming infinite.
α = Alpha parameter that adds weight to the FNs.
β = Beta parameter that adds weight to the FPs.

3.3 Accuracy assessment

3.3.1 Classical metrics

The model's prediction outputs are binary maps of landslide areas, which are then compared against manually mapped landslides (ground truth) using the Precision (equation 2), Recall (equation 3), and F1-score (equation 4) accuracy metrics. These metrics are calculated using True Positives (TPs), False Positives (FPs), and False Negatives (FNs), where, TPs are accurately identified landslide areas, FPs are non-landslide areas being detected as landslide areas, and FNs are landslide areas that were missed out by the model. *Precision* here refers to how well the model detects the landslide class. *Recall* is the number of times that the model detects the landslide class, and *F1-score* finally is the harmonic mean of (2) and (3) and acts as a balance between the two.

$$Precision = \frac{TP}{TP+FP} \qquad (2)$$

$$Recall = \frac{TP}{TP+FN} \ (3) \qquad\qquad F1 - score = 2 \times \frac{Precision \times Recall}{Precision + Recall} (4)$$

3.3.2 Landslide statistics and spatial distribution

The inventories used for training and validation were generated manually using visual image interpretation (See Table 1). Landslide statistics were evaluated for the manually annotated and predicted landslides for each respective year between 2013 and 2019 using information such as the total landslide area, maximum and minimum landslide area. Landslide densities were also analysed using the number of landslides per square kilometres in the different years. We used the kernel density toolset in GIS platform to create the landslide density hotspots. The kernel density toolset uses a moving counting kernel to determine density per unit area using point features generated by calculating the centroids of landslide polygons. The landslide density gives us an idea about the spatial location and changes in the spatial distribution of landslides over the years with the MT inventories.

4. Results and discussion

4.1 Multi-temporal landslide detection using U-Net

We compared the results against manually annotated landslides for accuracy assessment after using transfer learning for the different years. The model was evaluated on the test sets using the classical evaluation metrics of Precision, Recall, and F1-score, and using the change in landslide density. As discussed previously, we trained the model with landslides outside the investigation area (Figure 2) and tested on the investigation area of the year 2016 (one year after the Gorkha event). The results of the metrics can be seen in Table 2 and Figure 4. After that, we used transfer learning with pre-trained weights to re-train in our investigation area with newer landslide instances for each year from 2013 till 2019. In order to remove and filter out insignificant landslides detections by the model (which show a typical random effect of individual pixels in a so-called salt and pepper effect), we used a threshold area of 200 m^2 to filter out these isolated pixels, and thereby, cleaning the overall results.

Table 2: Table of various hyper-parameter combinations based on the preliminary training data and test data of 2017 (**bold** are the best combinations results).

Learning Rate	Number of filters	Batch Size	Loss	Precision	Recall	F1-score
1e-3	8	8	0.227	0.807	0.698	0.748
1e-3	16	8	0.218	0.817	0.702	0.755
1e-3	32	8	0.206	0.845	0.688	0.757
1e-3	8	16	0.229	0.805	0.701	0.749
1e-3	16	16	0.208	0.826	0.719	0.769
1e-3	32	16	0.226	0.865	0.618	0.721
1e-3	8	32	0.233	0.803	0.700	0.746
1e-3	16	32	0.205	0.824	0.725	0.771
1e-3	**32**	**32**	**0.188**	**0.850**	**0.731**	**0.785**
1e-4	8	8	0.559	0.710	0.678	0.694
1e-4	16	8	0.258	0.792	0.651	0.714
1e-4	32	8	0.220	0.821	0.699	0.755
1e-4	8	16	0.602	0.665	0.777	0.716
1e-4	16	16	0.325	0.791	0.607	0.687
1e-4	32	16	0.237	0.813	0.695	0.749
1e-4	8	32	0.584	0.000	0.000	0.000
1e-4	16	32	0.364	0.755	0.750	0.752
1e-4	32	32	0.242	0.818	0.702	0.755
1e-5	8	8	0.850	0.402	0.958	0.566
1e-5	16	8	0.753	0.547	0.892	0.678
1e-5	32	8	0.432	0.801	0.654	0.720
1e-5	8	16	0.838	0.332	0.955	0.493
1e-5	16	16	0.792	0.527	0.858	0.653
1e-5	32	16	0.509	0.754	0.753	0.752
1e-5	8	32	0.836	0.196	0.989	0.327
1e-5	16	32	0.813	0.477	0.898	0.623
1e-5	32	32	0.710	0.583	0.882	0.702

The appropriate combination of hyper-parameters allows the model to attain the optimal performance and thus to yield the highest possible mapping accuracy. As we see in Table 2, the best result of F1-score of 78.5% is achieved by the combinations of number of filters 32, batch size 32, and a learning rate of 0.001. This set of combinations were hence chosen for the re-train and testing using transfer learning on the other years inside the investigation area.

Based on numerous experiments for the optimal β value in the Tversky Loss function, β=0.7 proved best for the results of mapping the landslides over time. This is because setting β values higher than 0.7 give stronger attention on the FPs thus heavily reducing the Recall and/or reducing the Precision. In our study case, β=0.7 gave the best scores in terms of a balanced FP and FN, thereby mitigating the imbalance between Precision and Recall.

Table 3: Table of results for each year between 2013 and 2019 (using 32 filters, a batch size of 32 and a learning rate of 0.001).

Year	Loss	Precision	Recall	F1-score
2013	0.320	0.752	0.651	0.697
2014	0.165	0.762	0.696	0.727
2015	0.340	0.843	0.450	0.586
2016	0.205	0.927	0.603	0.731
2017	0.175	0.882	0.724	0.795
2018	0.290	0.753	0.633	0.688
2019	0.362	0.600	0.759	0.669

We can see in figure 4 the various landslide footprints that were detected by the model for the years between 2013 and 2019, tallied against the respective manually annotated landslide footprints.

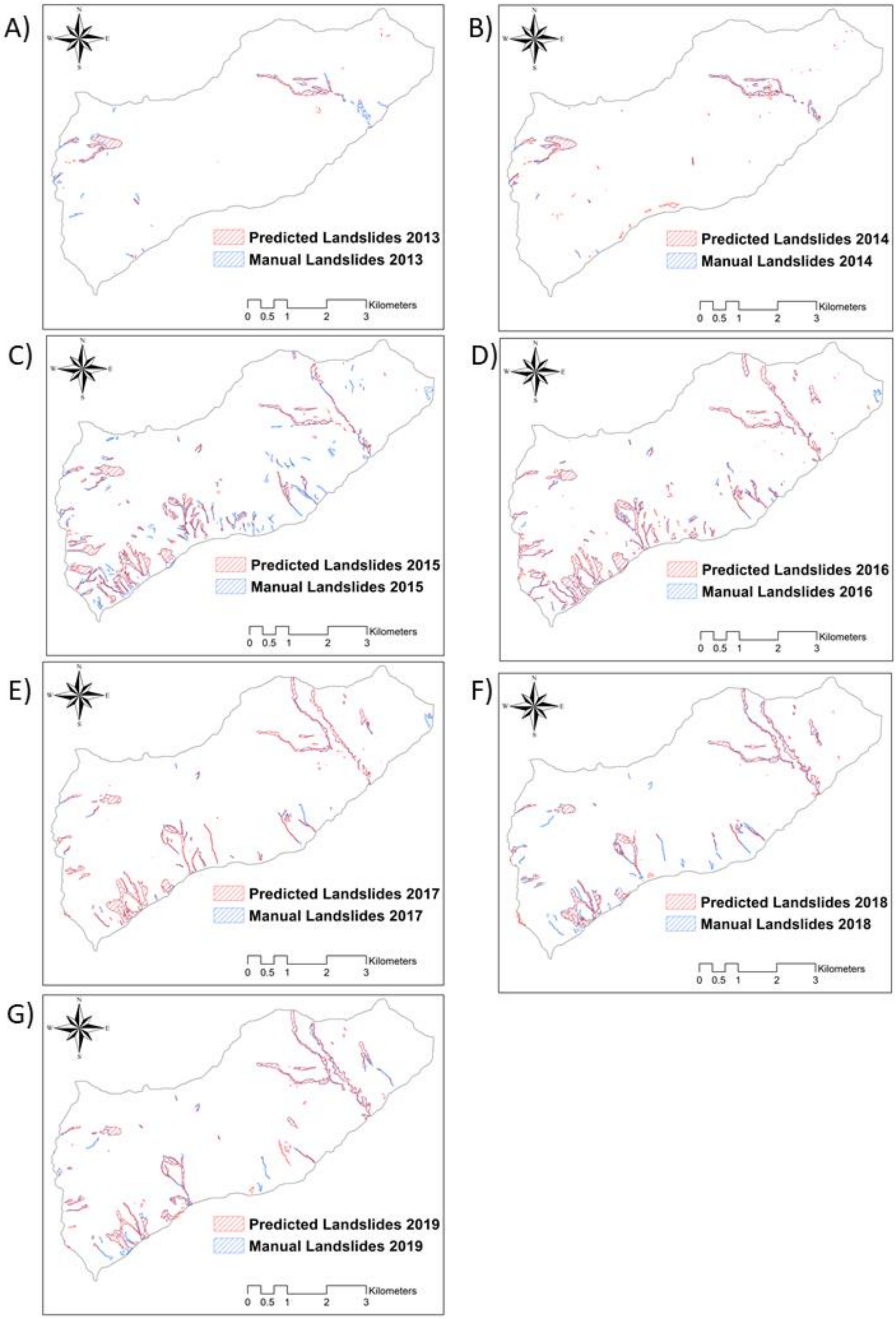
A)
Predicted Landslides 2013
Manual Landslides 2013
B)
Predicted Landslides 2014
Manual Landslides 2014
C)
Predicted Landslides 2015
Manual Landslides 2015
D)
Predicted Landslides 2016
Manual Landslides 2016
E)
Predicted Landslides 2017
Manual Landslides 2017
F)
Predicted Landslides 2018
Manual Landslides 2018
G)
Predicted Landslides 2019
Manual Landslides 2019
0 0.5 1 2 3
Kilometers

Figure 4: Predicted landslides versus the manually delineated landslides of the years 2013 till 2019.

4.2 Comparing the spatial distribution of manual (observed) and predicted landslides

The spatial distributions of the manual and predicted landslide polygons were compared with landslide statistics and landslide density (LD) for each year. The findings are presented in Table 4.

Table 4: Comparison of landslide statistics for the manually mapped landslide inventories versus the predicted ones.

Year	Manually Annotated Landslide Inventory (MI)				Predicted Landslide Inventory (PI)			
	Total number of landslides (T_L)	Total area of landslides ($T\ A_L$) in m²	Minimum area of landslides ($Min\ A_L$) in m²	Maximum area of landslides ($Max\ A_L$) in m²	Total number of landslides (T_L) in m²	Total area of landslides ($T\ A_L$) in m²	Minimum area of landslides ($Min\ A_L$) in m²	Maximum area of landslides ($Max\ A_L$) in m²
2013	31	513,304.8	216.3	148,948.1	38	369,595.9	215.24	186,958
2014	26	438,778.5	515.7	150,759.3	53	437,334.0	206.1	170,278
2015	136	1,855,911.8	276.4	145,380.5	108	1,336,636.5	264.0	224,417
2016	95	1,796,221.2	768.3	137,397.8	117	1,633,912.1	202.6	405,951
2017	63	1,188,037.6	724.5	141,102.3	73	1,048,197.0	217.1	255,057
2018	55	1,315,124.4	724.5	141,102.3	75	1,011,351.6	202.6	254,061
2019	52	1,222,396.5	724.5	112,723.0	87	1,036,097.9	214.6	155,752

Table 4 shows that the minimum landslide area is almost always around 200 m², as this values was chosen as threshold to avoid mapping of individual pixels. A single landslide in the manual interpretation can sometimes be predicted as multiple instances in the predicted inventory, as the possible functional connection between them (e.g. along a debris flow channel) cannot be analyzed automatically. This is a very common issue as seen in the works of Prakash et al. (2021) and Zhang, Pun, and Liu (2021) and thus post-processing approaches should be employed to reduce the problem. The opposite is also witnessed in the inventories of 2015 where we see that MI had a higher number of landslides than PI. The reason behind this is the fact that some landslides were not detected by the model, as explained in the low F1-score of 58.6% (Table 3), thereby resulting in lower T_L. However, the $Max\ A_L$ and the $T\ A_L$ give a more positive and optimistic overview of the detected landslides in general, since they are comparable across all the investigated years. Moreover, we also obtained more landslides that are actually missing in the inventory, and therefore, the additional area seen in Table 4 is actually more representative. Interestingly, we also notice that the trend of the total number of landslides (T_L) is quite similar between MI and PI. The number of landslides increases in 2015 as a result of the Gorkha earthquake, then gradually declines in the subsequent years. This observation is in line with recent post-seismic landslide evolution studies (Fan et al., 2021). We can also notice that the areas and number of active landslides between MI and PI are different. This can be attributed to the previously discussed fragmentation problem in terms of the model predictions. Table 3 reflects varying results in the F1-scores, although from a spatial point of view, they are related to the same area. This is because the image acquisitions, even in the same seasons (late autumn and early winter), have different spectral reflectance/atmospheric disturbances, which confuse the model even while predicting the same landslides repeatedly. The image of 2015 was the most different spectrally, and that’s why we see in

Table 3 that the best F1-score is only 58%. However, for the other years, the F1-scores varies between 65% and 80%.

Figure 6 illustrates the problems discussed above for the year 2015 where the landslide detections are relatively poor compared against the rest. Many landslides seem to be missing in the centre and the eastern part of the area, which is indicative of the poor F1-score of 58%. This explains the lower value of T_L in Table 4 for the predicted inventory (108) against the manual inventory (136). As discussed previously, this can occur because of the observed differences in the spectral reflectance which reduces the efficiency of the model to predict the landslides of 2015. Much better predictions are observed in the south-western part of the map where the landslides are mapped almost identically. However, a substantial number of landslides are also missed out in the eastern part of the map for the years 2013, 2015, and 2019. Overall, the prediction over the different years very well captures the general location of the landslide footprints and gives a positive outlook towards employing DL methods for MT inventory generation.

To analyse the landslide density (LD) per square kilometre, we used the centroid of each landslide polygon. We used landslide inventory datasets from 2013-2019 obtained from satellite images for the same season after the monsoon. Based on the results in Table 4, variation in the total number of landslides as well as landslide area can be seen in the manual and predicted inventories. Total area of landslides (TA_L) in manual inventories ranges from 438,778.5 m² to 1,855,911.8 m² and for the predicted ones, it ranges from 369,595.9 m² to 1,633,912.1 m². Moreover, the smallest and largest mapped landslide polygon varies as well, both for the manual and predicted inventories (Table 4). To understand the variations in the spatial distribution of the inventories across the years, a landslide density (LD) analysis was performed for both manual and predicted inventories. The LD distribution varies for manual and predicted inventories ranging between 3.22 and 2.59 landslides/km², respectively, in the year 2013. After 2015 earthquake event, the landslide density increased to 16.46 landslides/km² and 11.47/km² for the manual and predicted inventories, respectively. The trend for LD distribution for the same area declined after 2016 for the manual inventory and the same is observed for the predicted inventory (Table 5).

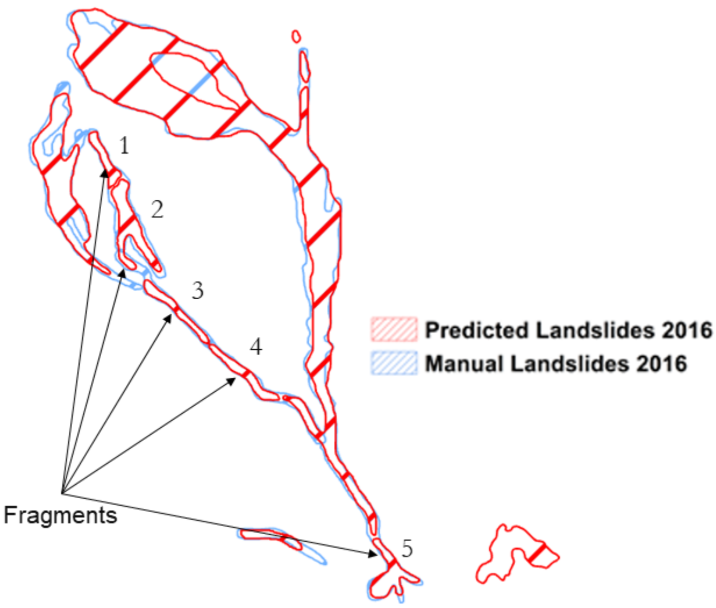

Figure 5: Fragmentation of the landslides of the predicted inventories (red) compared to the manual inventories (blue).

For two cases (2013 and 2015), the landslide density of the predicted landslide inventories is lower than the manual inventories while, for the rest of the years it is the opposite. While for 2013 the difference is relatively small (-0.63), this is much larger in 2015 (-4.99) as seen in Table 5. In 2015, the overall prediction is weaker when compared to the other years. In fact, since the Recall is around 45% (Table 3) for 2015, most of the landslide pixels were missed out by the model.

However, for the year 2016, we observe that the LD of PI is higher than that of MI, showing a positive difference of 3.17. Notice that after the event in 2015, the LD of MI decreased (as expected due to re-vegetation in the terrain) from 16.46 to 8.37 but this behaviour was not reflected in PI as the LD remained almost the same. This phenomenon can be explained by the fragmented predictions made by the model as illustrated in Figure 5. As the model predictions are pixel-based, landslide bodies may be predicted in portions. Thus, a single landslide body can be fragmented into two or more bodies yielding more portions for the same landslide body. This phenomenon leads towards an increase in the overall number of landslides per km^2. Like T_L, the overall trend of the LD for both MI and PI are similar where we first see an increase in the density in 2015 followed by decrease in the following years (except for the 2016 outlier for P).

Table 5: Comparison of landslide density for the manually annotated landslide inventories versus the predicted landslide inventories.

Years	Density of the manual landslide inventory MI (Nr / km^2)	Density of the predicted landslide inventory PI (Nr / km^2)	Difference (PI - MI) (Nr / km^2)
2013	3.22	2.59	-0.63
2014	3.62	6.64	3.02
2015	16.46	11.47	-4.99
2016	8.37	11.54	3.17
2017	6.16	7.46	1.30
2018	4.85	7.35	2.50
2019	4.70	6.99	2.25

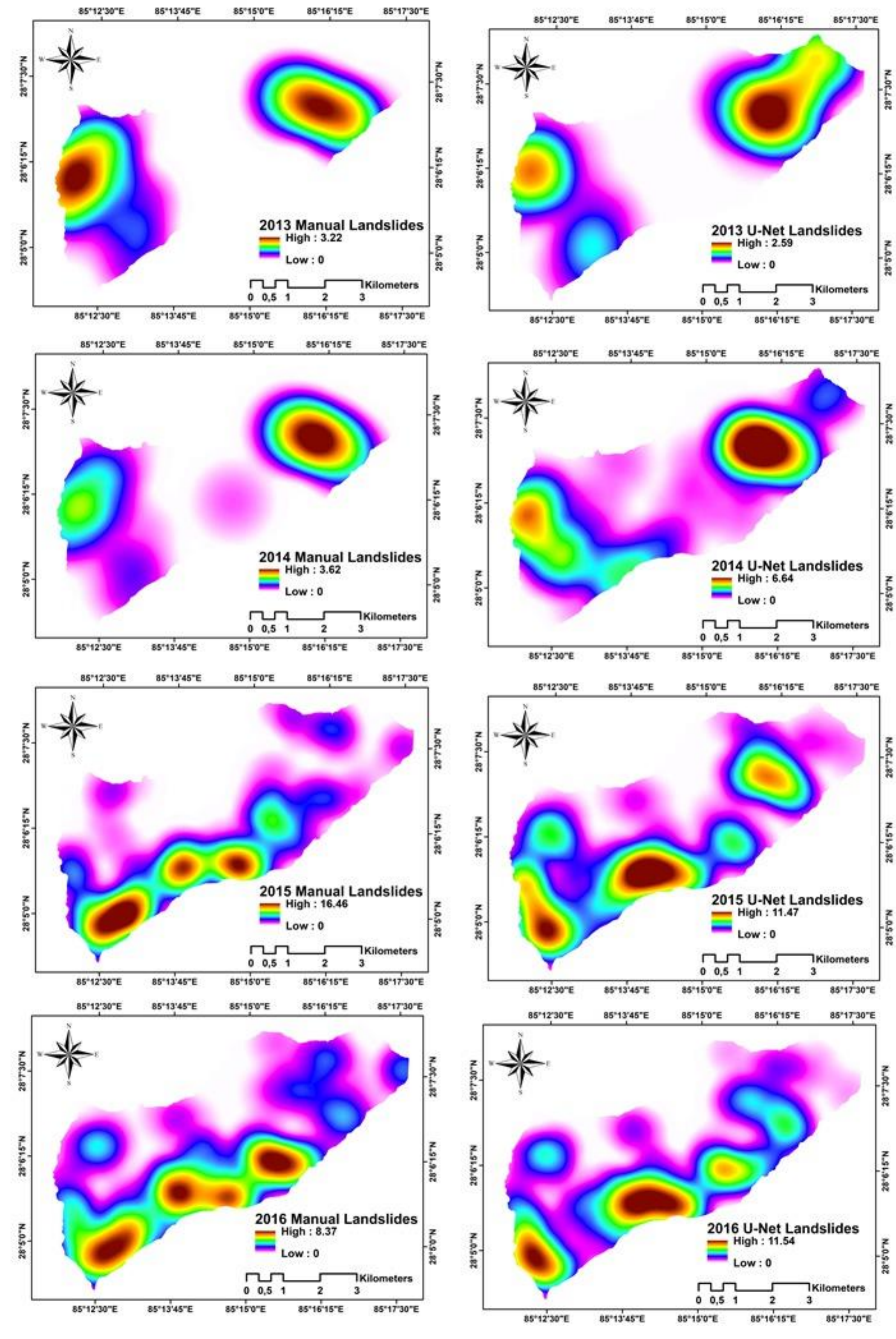
2013 Manual Landslides
High : 3.22
Low : 0
2013 U-Net Landslides
High : 2.59
Low : 0
2014 Manual Landslides
High : 3.62
Low : 0
2014 U-Net Landslides
High : 6.64
Low : 0
2015 Manual Landslides
High : 16.46
Low : 0
2015 U-Net Landslides
High : 11.47
Low : 0
2016 Manual Landslides
High : 8.37
Low : 0
2016 U-Net Landslides
High : 11.54
Low : 0
Kilometers
0 0,5 1 2 3
85°12'30"E
85°13'45"E
85°15'0"E
85°16'15"E
85°17'30"E
28°7'30"N
28°6'15"N
28°5'0"N

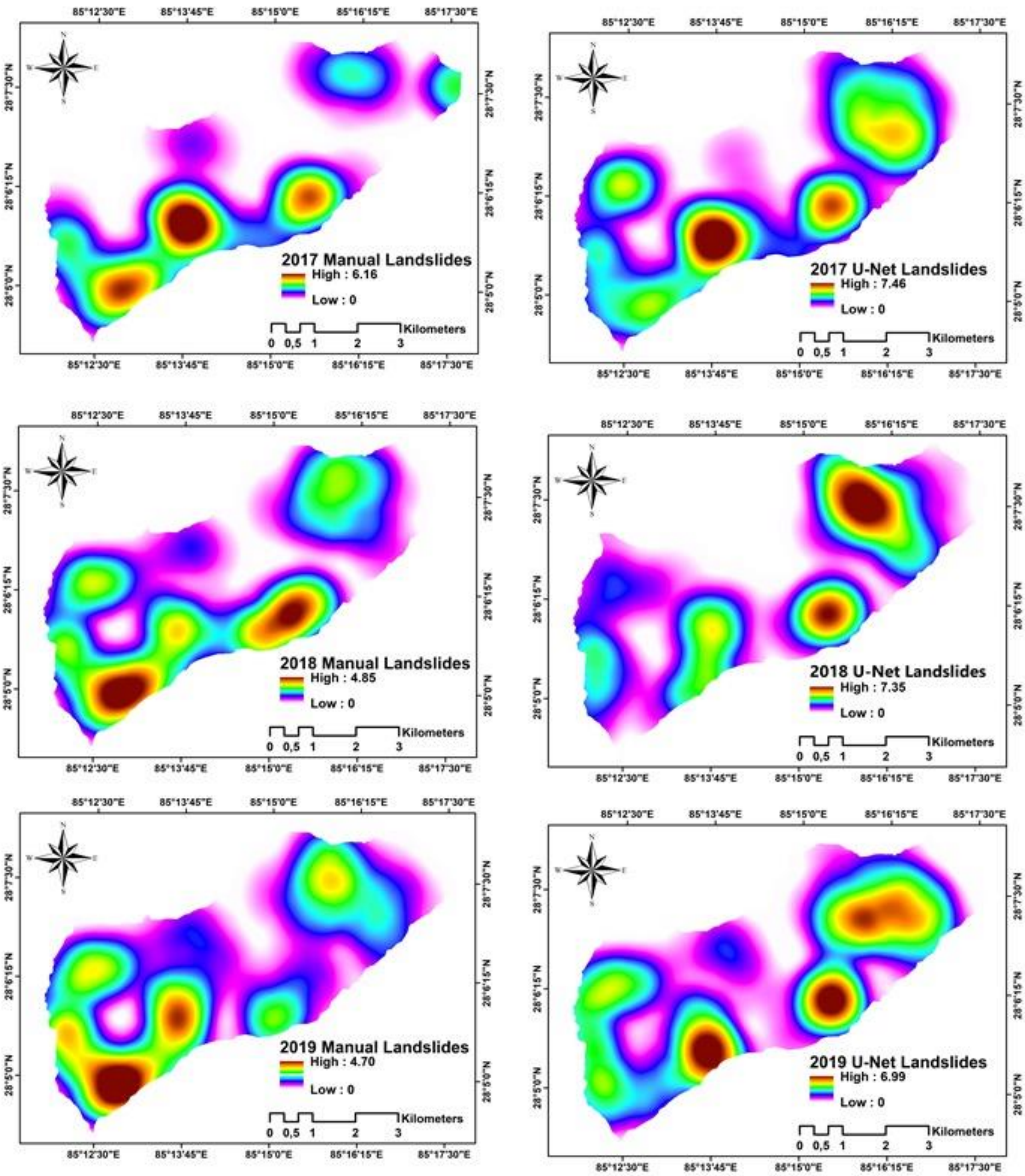

Figure 6: The density of the landslides of the manually annotated versus the predicted inventories for the year 2013 till 2019.

5. Conclusions

Mapping landslides automatically is a difficult task and much research has been conducted that shows how well DL models can be used to map landslides efficiently and rapidly. But this mapping endeavour through DL models is thus far only explored spatially, and not temporally. We propose the first multi-temporal landslide inventory mapping effort with the U-Net DL model to automatically detect and map landslides over time by using medium resolution RapidEye images of the Nepal Mailung area for the years between 2013 and 2019. The U-Net model is first trained separately outside the investigation area to test model effectiveness in a geographically distinct area and then the weights learnt from this first training phase are utilised to map landslides over time within the investigation area using transfer learning. The model's performance is assessed using classical metrics on the test set, as well as differences in spatial distribution and landslide statistics between the manual and modelled inventories.

A typical issue in the successful implementation of a data-driven model for landslide mapping tasks is the shortage of training data. Although the use of 55 training samples can be usually judged as very small for effective training of a deep learning model, it has shown itself effective in our study by applying data augmentation techniques to expand the amount of training samples, thereby allowing the model to generalise better in predicting landslides temporally. A major challenge faced has been the spectral reflectance differences between each image acquisition for each year. Results show that for each year, the overall F1-scores are different because of these variations in the spectral reflectance for each year, however, in general, the landslide footprints are mapped very well for each year. The results also show that using training samples of only 55 landslides from a geographically separate area is enough to detect landslides temporally in interested regions, and also to get more than adequate accuracies to generate MT inventories. Various gaps and constraints remain despite the fact that this is the first study to attempt in MT mapping of landslides. Among them: i) the choice of seasonality has to be investigated further, as it is responsible for significant spectral changes in imagery, mostly linked to vegetation.; ii) determining landslide footprints of each respective year while avoiding double counting.

Our next focus will be on attempting to detect and map multi-temporal landslides over different topographic regions in order to test how well such models perform in terms of their generalisation capability. Moreover, different models will also be experimented to utilize more advanced networks and layers at improving the mapping of landslide footprints.

6. Data and code availability

We present the data and codes openly available at https://github.com/kushanavbhuyan/Multi-Temporal-Landslide-Mapping-Nepal to encourage reproducibility of the study. We include a Jupyter Notebook script and the trained model weights, making it straightforward for interested academics to design and test MT landslide inventories in new regions of interest.

Declarations

Conflict of Interest

The authors affirm that there are no conflicts of interest linked with this study.

Author Agreement

As the corresponding Author, I certify that this manuscript is unique, has never been published, and is not under consideration for publication anywhere else. I certify that all listed authors have read and approved the work. I also confirm that we have all given our permission to the authorship order shown in the text.

Author Contributions: Conceptualization, K.B., and S.R.M.; data curation, S.R.M, methodology, K.B; analysis and interpretation of results, K.B., S.R.M., and L.N.; ; writing—original draft preparation, K.B., and L.N.; writing, review and editing, S.R.M., K.B., L.N., C.V.W., M.F., and F.C.; supervision, C.V.W., M.F., and F.C.; funding acquisition, K.B. The published version of the work has been reviewed and approved by all authors.

Funding: This research received no external funding.

References

Abraham, N., & Khan, N. M. (2019). A novel focal tversky loss function with improved attention u-net for lesion segmentation. *Proceedings - International Symposium on Biomedical Imaging*, *2019-April*, 683–687. IEEE Computer Society. https://doi.org/10.1109/ISBI.2019.8759329

Anderson, J. E., & Perry, J. E. (1996). Characterization of wetland plant stress using leaf spectral reflectance: Implications for wetland remote sensing. *Wetlands 1996 16:4*, *16*(4), 477–487. https://doi.org/10.1007/BF03161337

Bai, S., Wang, J., Zhang, Z., & Cheng, C. (2012). Combined landslide susceptibility mapping after Wenchuan earthquake at the Zhouqu segment in the Bailongjiang Basin, China. *CATENA*, *99*, 18–25. https://doi.org/10.1016/J.CATENA.2012.06.012

Bottou, L. (2010). Large-scale machine learning with stochastic gradient descent. In *Proceedings of COMPSTAT 2010 - 19th International Conference on Computational Statistics, Keynote, Invited and Contributed Papers* (pp. 177–186). Physica-Verlag HD. https://doi.org/10.1007/978-3-7908-2604-3_16

Catani, F. (2021). Landslide detection by deep learning of non-nadiral and crowdsourced optical images. *Landslides*, *18*(3), 1025–1044. https://doi.org/10.1007/s10346-020-01513-4

Fan, X., Scaringi, G., Domènech, G., Yang, F., Guo, X., Dai, L., … Huang, R. (2019, January 9). Two multi-temporal datasets that track the enhanced landsliding after the 2008 Wenchuan earthquake. *Earth System Science Data*, Vol. 11, pp. 35–55. Copernicus GmbH. https://doi.org/10.5194/essd-11-35-2019

Fan, X., Xu, Q., van Westen, C. J., Huang, R., & Tang, R. (2017). Characteristics and classification of landslide dams associated with the 2008 Wenchuan earthquake. *Geoenvironmental Disasters*, *4*(1), 1–15. https://doi.org/10.1186/s40677-017-0079-8

Fan, X., Yunus, A. P., Scaringi, G., Catani, F., Siva Subramanian, S., Xu, Q., & Huang, R. (2021, January 16). Rapidly Evolving Controls of Landslides After a Strong Earthquake and Implications for Hazard Assessments. *Geophysical Research Letters*, Vol. 48, p. e2020GL090509. John Wiley & Sons, Ltd. https://doi.org/10.1029/2020GL090509

Fang, B., Chen, G., Pan, L., Kou, R., & Wang, L. (2021). GAN-Based Siamese Framework for Landslide Inventory Mapping Using Bi-Temporal Optical Remote Sensing Images. *IEEE Geoscience and Remote Sensing Letters*, *18*(3), 391–395. https://doi.org/10.1109/LGRS.2020.2979693

Ghorbanzadeh, O., Blaschke, T., Gholamnia, K., Meena, S. R., Tiede, D., & Aryal, J. (2019). Evaluation of different machine learning methods and deep-learning convolutional neural networks for landslide detection. *Remote Sensing*, *11*(2), 196. https://doi.org/10.3390/rs11020196

Ghorbanzadeh, O., Crivellari, A., Ghamisi, P., Shahabi, H., & Blaschke, T. (2021). A comprehensive transferability evaluation of U-Net and ResU-Net for landslide detection from Sentinel-2 data (case study areas from Taiwan, China, and Japan). *Scientific Reports*, *11*(1). https://doi.org/10.1038/s41598-021-94190-9

Ghorbanzadeh, O., Meena, S. R., Shahabi Sorman Abadi, H., Tavakkoli Piralilou, S., Zhiyong, L., & Blaschke, T. (2021a). Landslide Mapping Using Two Main Deep-Learning Convolution Neural Network Streams Combined by the Dempster-Shafer Model. *IEEE Journal of Selected Topics in Applied Earth Observations and Remote Sensing*, *14*, 452–463. https://doi.org/10.1109/JSTARS.2020.3043836

Ghorbanzadeh, O., Meena, S. R., Shahabi Sorman Abadi, H., Tavakkoli Piralilou, S., Zhiyong, L., & Blaschke, T. (2021b). Landslide Mapping Using Two Main Deep-Learning Convolution Neural Network Streams Combined by the Dempster-Shafer Model. *IEEE Journal of Selected Topics in*

Applied Earth Observations and Remote Sensing, *14*, 452–463. https://doi.org/10.1109/JSTARS.2020.3043836

Guzzetti, F., Reichenbach, P., Cardinali, M., Galli, M., & Ardizzone, F. (2005). Probabilistic landslide hazard assessment at the basin scale. *Geomorphology*, *72*(1–4), 272–299. https://doi.org/10.1016/j.geomorph.2005.06.002

Huete, A. R. (2004). REMOTE SENSING FOR ENVIRONMENTAL MONITORING. *Environmental Monitoring and Characterization*, 183–206. https://doi.org/10.1016/B978-012064477-3/50013-8

Jaiswal, P., & van Westen, C. J. (2009). Estimating temporal probability for landslide initiation along transportation routes based on rainfall thresholds. *Geomorphology*, *112*(1–2), 96–105. https://doi.org/10.1016/j.geomorph.2009.05.008

Kargel, J. S., Leonard, G. J., Shugar, D. H., Haritashya, U. K., Bevington, A., Fielding, E. J., … Young, N. (2016). Geomorphic and geologic controls of geohazards induced by Nepal's 2015 Gorkha earthquake. *Science*, *351*(6269). https://doi.org/10.1126/SCIENCE.AAC8353/SUPPL_FILE/KARGEL-SM.PDF

Kukačka, J., Golkov, V., & Cremers, D. (2017). *Regularization for Deep Learning: A Taxonomy*. Retrieved from https://arxiv.org/abs/1710.10686v1

Martha, T. R., Roy, P., Mazumdar, R., Govindharaj, K. B., & Kumar, K. V. (2016). Spatial characteristics of landslides triggered by the 2015 Mw 7.8 (Gorkha) and Mw 7.3 (Dolakha) earthquakes in Nepal. *Landslides 2016 14:2*, *14*(2), 697–704. https://doi.org/10.1007/S10346-016-0763-X

Meena, S. R., Ghorbanzadeh, O., van Westen, C. J., Nachappa, T. G., Blaschke, T., Singh, R. P., & Sarkar, R. (2021). Rapid mapping of landslides in the Western Ghats (India) triggered by 2018 extreme monsoon rainfall using a deep learning approach. *Landslides*, *18*(5), 1937–1950. https://doi.org/10.1007/s10346-020-01602-4

Meena, S. R., & Piralilou, S. T. (2019). Comparison of Earthquake-Triggered Landslide Inventories: A Case Study of the 2015 Gorkha Earthquake, Nepal. *Geosciences 2019, Vol. 9, Page 437*, *9*(10), 437. https://doi.org/10.3390/GEOSCIENCES9100437

Meena, S. R., Soares, L. P., Grohmann, C. H., van Westen, C., Bhuyan, K., Singh, R. P., … Catani, F. (2022). Landslide detection in the Himalayas using machine learning algorithms and U-Net. *Landslides*. https://doi.org/10.1007/s10346-022-01861-3

Metternicht, G., Hurni, L., & Gogu, R. (2005). Remote sensing of landslides: An analysis of the potential contribution to geo-spatial systems for hazard assessment in mountainous environments. *Undefined*, *98*(2–3), 284–303. https://doi.org/10.1016/J.RSE.2005.08.004

Pan, Z., Xu, J., Guo, Y., Hu, Y., & Wang, G. (2020). Deep learning segmentation and classification for urban village using a worldview satellite image based on U-net. *Remote Sensing*, *12*(10), 1574. https://doi.org/10.3390/rs12101574

Planet Team. (2017). *Planet Application Program Interface: In Space for Life on Earth*. https://doi.org/https://api.planet.com

Prakash, N., Manconi, A., & Loew, S. (2020). Mapping landslides on EO data: Performance of deep learning models vs. Traditional machine learning models. *Remote Sensing*, *12*(3). https://doi.org/10.3390/rs12030346

Prakash, N., Manconi, A., & Loew, S. (2021). A new strategy to map landslides with a generalized convolutional neural network. *Scientific Reports*, *11*(1), 1–15. https://doi.org/10.1038/s41598-021-89015-8

Roback, K., Clark, M. K., West, A. J., Zekkos, D., Li, G., Gallen, S. F., … Godt, J. W. (2018). The size, distribution, and mobility of landslides caused by the 2015 Mw7.8 Gorkha earthquake, Nepal. *Geomorphology*, *301*, 121–138. https://doi.org/10.1016/J.GEOMORPH.2017.01.030

Ronneberger, O., Fischer, P., & Brox, T. (2015). U-net: Convolutional networks for biomedical image segmentation. *Lecture Notes in Computer Science (Including Subseries Lecture Notes in Artificial Intelligence and Lecture Notes in Bioinformatics)*, *9351*, 234–241. Springer Verlag. https://doi.org/10.1007/978-3-319-24574-4_28

Rosser, N., Kincey, M., Oven, K., Densmore, A., Robinson, T., Pujara, D. S., … Dhital, M. R. (2021). Changing significance of landslide Hazard and risk after the 2015 Mw 7.8 Gorkha, Nepal Earthquake. *Progress in Disaster Science*, *10*, 100159. https://doi.org/10.1016/j.pdisas.2021.100159

Samia, J., Temme, A., Bregt, A., Wallinga, J., Guzzetti, F., Ardizzone, F., & Rossi, M. (2017). Do landslides follow landslides? Insights in path dependency from a multi-temporal landslide inventory. *Landslides*, *14*(2), 547–558. https://doi.org/10.1007/s10346-016-0739-x

Schwanghart, W., Ryan, M., & Korup, O. (2018). Topographic and Seismic Constraints on the Vulnerability of Himalayan Hydropower. *Geophysical Research Letters*, *45*(17), 8985–8992. https://doi.org/10.1029/2018GL079173

Serey, A., Piñero-Feliciangeli, L., Sepúlveda, S. A., Poblete, F., Petley, D. N., & Murphy, W. (2019). Landslides induced by the 2010 Chile megathrust earthquake: a comprehensive inventory and correlations with geological and seismic factors. *Landslides 2019 16:6*, *16*(6), 1153–1165. https://doi.org/10.1007/S10346-019-01150-6

Shorten, C., & Khoshgoftaar, T. M. (2019). A survey on Image Data Augmentation for Deep Learning. *Journal of Big Data*, *6*(1), 1–48. https://doi.org/10.1186/S40537-019-0197-0/FIGURES/33

Soeters, R., & Van Westen, C. J. (1996). Slope instability recognition, analysis, and zonation. *Special Report - National Research Council, Transportation Research Board*, *247*, 129–177. https://doi.org/10.2/JQUERY.MIN.JS

Sreedevi, N., & Yarrakula, K. (2016). Different Techniques for Landslide Zonation Mapping and Landslide Assessment: A Review. *Indian Journal of Science and Technology*, *9*(47). https://doi.org/10.17485/IJST/2015/V8I1/106518

Tang, C., Van Westen, C. J., Tanyas, H., & Jetten, V. G. (2016). Analysing post-earthquake landslide activity using multi-temporal landslide inventories near the epicentral area of the 2008 Wenchuan earthquake. *Natural Hazards and Earth System Sciences*, *16*(12), 2641–2655. https://doi.org/10.5194/nhess-16-2641-2016

Tanyaş, H., Kirschbaum, D., Görüm, T., van Westen, C. J., & Lombardo, L. (2021). New Insight into Post-seismic Landslide Evolution Processes in the Tropics. *Frontiers in Earth Science*, *9*, 551. https://doi.org/10.3389/feart.2021.700546

Van Westen, C. J., Ghosh, S., Jaiswal, P., Martha, T. R., & Kuriakose, S. L. (2013). From Landslide Inventories to Landslide Risk Assessment; An Attempt to Support Methodological Development in India. *Landslide Science and Practice: Landslide Inventory and Susceptibility and Hazard Zoning*, *1*, 3–20. https://doi.org/10.1007/978-3-642-31325-7_1

Wang, F., Fan, X., Yunus, A. P., Siva Subramanian, S., Alonso-Rodriguez, A., Dai, L., … Huang, R. (2019). Coseismic landslides triggered by the 2018 Hokkaido, Japan (Mw 6.6), earthquake: spatial distribution, controlling factors, and possible failure mechanism. *Landslides 2019 16:8*, *16*(8), 1551–1566. https://doi.org/10.1007/S10346-019-01187-7

Xu, C., Xu, X., Dai, F., Wu, Z., He, H., Shi, F., … Xu, S. (2013). Application of an incomplete landslide inventory, logistic regression model and its validation for landslide susceptibility mapping related to the May 12, 2008 Wenchuan earthquake of China. *Natural Hazards*, *68*(2), 883–900. https://doi.org/10.1007/S11069-013-0661-7/FIGURES/7

Xu, C., Xu, X., Yao, X., & Dai, F. (2014). Three (nearly) complete inventories of landslides triggered by the May 12, 2008 Wenchuan Mw 7.9 earthquake of China and their spatial distribution statistical analysis. *Landslides*, *11*(3), 441–461. https://doi.org/10.1007/S10346-013-0404-6/TABLES/4

Zhang, X., Pun, M. O., & Liu, M. (2021). Semi-supervised multi-temporal deep representation fusion network for landslide mapping from aerial orthophotos. *Remote Sensing*, *13*(4), 1–22. https://doi.org/10.3390/rs13040548

Zhang, Z., Liu, Q., & Wang, Y. (2018). Road Extraction by Deep Residual U-Net. *IEEE Geoscience and Remote Sensing Letters*, *15*(5), 749–753. https://doi.org/10.1109/LGRS.2018.2802944